Continuous-wave amplification and light storage in optically and electrically pumped random laser media

Bin Li and Stephen C. Rand

Department of Electrical Engineering and Computer Science, University of Michigan, Ann Arbor, Michigan 48109-2122, USA

Received May 18, 2006; revised November 7, 2006; accepted November 13, 2006; posted December 8, 2006 (Doc. ID 71108); published March 15, 2007

Gain competition is analyzed theoretically on coupled stimulated emission transitions in Λ-type configurations of excited atoms and compared with experimental observations in electrically and optically pumped random media. Under steady-state conditions, we predict and observe dramatic spectral quenching among $^2F_{5/2}$ transitions in electron-beam-irradiated Nd^{3+}:δ-Al_2O_3 nanopowders, identifying a simple mechanism that promotes laser action at the longest wavelength (405 nm). In optically pumped Nd^{3+}:Y_2O_3 nanopowder, simultaneous laser action is observed at two previously unreported wavelengths of Nd^{3+} (763 and 821 nm), but spectral quenching is not observed, owing to the absence of Λ coupling among the inverted transitions. Quantitative analysis of quenching and threshold behavior in the case of Nd^{3+}:δ-Al_2O_3 indicates that in wavelength-sized volumes of these light-confining media the average storage time of light may be as long as 30 ps. © 2007 Optical Society of America

OCIS codes: 140.5680, 140.3380, 140.3530.

1. INTRODUCTION

Random lasers have been studied intensively since the earliest reports of stimulated emission in strongly scattering media, to explore their unusual properties, mechanisms, and potential applications. Pulsed random lasers have been demonstrated in a wide variety of media including powdered rare-earth crystals,[1–3] organic dyes in suspensions of scatterers,[4] polymers incorporating scattering centers,[5] nanocrystalline semiconductors,[6,7] and other systems. Numerous investigations have been carried out on the theoretical[8,9] and experimental mode structure[10] and coherence properties[11,12] of these intriguing light sources. By contrast, there are only a few reports of continuous-wave (cw) random lasing.[13–16] The apparent absence of mode structure and coherence in the latter case has hindered analysis of the lasing mechanism and cavity properties. Recent experiments[16] on cw laser output versus penetration depth of incident electrons in Nd^{3+}:δ-Al_2O_3 confirm that the effective transport length contributing to confinement in the random laser medium is of the order of the optical wavelength (λ) along the normal to the sample surface. With a mean transport length also measured to be approximately equal to the wavelength of light, mode discrimination within the cavity is prohibited, thereby accounting in principle for the absence of mode structure. As yet, however, no detailed analysis of the quenching of sample luminescence near laser threshold reported in Ref. 15 has been presented. Nor have additional examples of cw laser action emerged. In this paper, we present both detailed analysis of earlier results (Fig. 1) and new examples, to our knowledge, of cw random laser action.

Stimulated emission dynamics of dopant ions in a random dielectric are analyzed theoretically here for coupled transitions in Λ-type atomic configurations, and the observed spectral characteristics and threshold behavior of cw Nd^{3+}:δ-Al_2O_3 and Nd^{3+}:Y_2O_3 random lasers are thereby explained. Detailed analysis of coupled transitions in Nd^{3+}:δ-Al_2O_3 yields the average cavity size and storage time for laser light generated in small feedback regions of the active medium. Optically pumped laser action is also shown to take place in Nd^{3+}:Y_2O_3 at 763 and 821 nm simultaneously (Fig. 2), on uncoupled transitions.

The mechanism and dimensionality of light confinement within active random dielectric scattering media are also addressed in this paper. The refractive indices of dielectric materials such as Al_2O_3 and Y_2O_3 have previously been thought to be too low to lead directly to Anderson localization of light by uncorrelated scattering interactions in three dimensions.[17] It was shown recently, though, that correlated multiple scattering in inhomogeneous random systems leads to the coexistence of localized and delocalized modes in one-dimensional low-index dielectrics,[16,18] so that our understanding of correlation and gain effects on three-dimensional dynamics may be incomplete. In the present paper, field correlations and optical gain are shown to mediate strong, quasi-one-dimensional localization that is adequate to sustain cw laser action in low-gain media through nonlocal interference effects unassociated with specific (local) structures. The optical dynamics on laser transitions in Nd^{3+}-doped nanopowders[15] are confirmed to be entirely consistent with the key properties shared by all laser oscillators, namely, stimulated emission with cavity feedback and linear output. The use of one-dimensional analysis is discussed and justified for low-gain three-dimensional me-

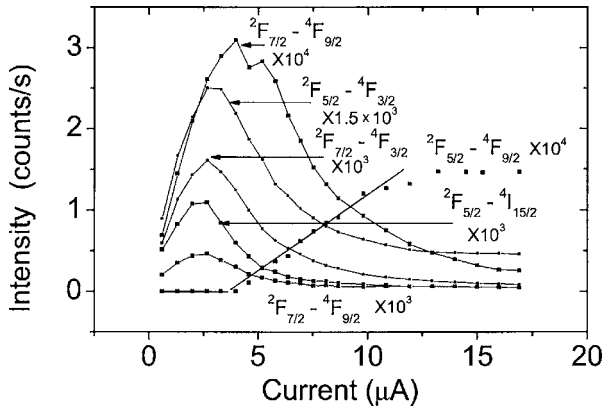

Fig. 1. Luminescence intensities versus electron-beam current in Nd^{3+}:δ-Al_2O_3 nanopowder. Note the sharp threshold on only one transition, namely, the $^2F_{5/2}$–$^4F_{9/2}$ transition, and dramatic spectral quenching on all other transitions (from the ^2F upper states).

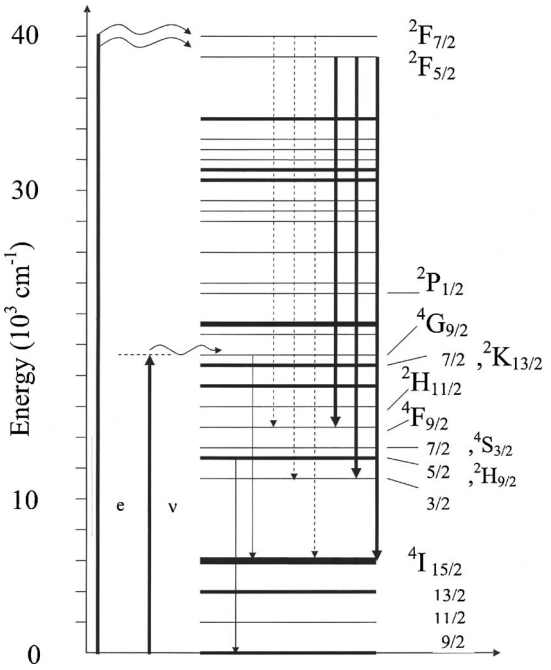

Fig. 2. Energy levels of Nd^{3+}. Bold upward arrows show electron (e) and photon (ν) excitation pathways. Bold downward arrows correspond to the three coupled transitions whose quenching behavior in Nd^{3+}:Al_2O_3 is analyzed in the text. Dashed arrows indicate $^2F_{7/2}$ transitions whose dynamics parallel those of the $^2F_{5/2}$ transitions because of thermal equilibrium between the upper states. Thin downward arrows are transitions observed in Nd^{3+}:Y_2O_3.

dia, and observations of spectral dynamics are fully explained. We account theoretically for gain competition curves, threshold behavior, and threshold pump rate of the Nd^{3+}:δ-Al_2O_3 random laser. We determine the average size of Nd^{3+}:δ-Al_2O_3 laser cavities to be $l_c = (1.6 \pm 1.0)\lambda$, in agreement with values inferred from previous backscattering data[13] and electron penetration experiments.[16] Finally, stimulated emission dynamics of optically pumped Nd^{3+} ions in Y_2O_3 nanopowder at 763 and 821 nm are reported and compared with Nd^{3+}:δ-Al_2O_3 results. This provides the most detailed picture yet of continuous generation and storage of laser light in a strongly scattering random gain medium.

2. THEORY

In conventional lasers it is well known that large, wavelength-selective cavities favor stimulated emission in a single resonant mode. The mode intensity grows linearly above laser threshold, and light emission at wavelengths not in resonance with cavity feedback exhibits a constant intensity above threshold, as the result of clamping of the upper-state population on the laser transition.[19] These qualitative features are reproduced by even the simplest laser model. For a laser with an empty terminal state, the population N of the initial level constitutes the entire inversion, and laser behavior can be modeled with a single equation for the excited-state population N and one for the photon density n inside the cavity. For a linear resonator with cavity and radiative lifetimes τ_c and τ, respectively, we have

$$\dot{N} = R_p - KNn - N/\tau, \tag{1.1}$$

$$\dot{n} = K(n+1)N - n/\tau_c. \tag{1.2}$$

Here R_p is the pumping rate, and $K = \hbar\omega c B/V_c$ is a constant that depends on the frequency ω, the Einstein B coefficient, and cavity volume V_c. $\dot{N} \equiv \partial N/\partial t$, and $\dot{n} \equiv \partial n/\partial t$. Although Eqs. (1.1) and (1.2) are coupled nonlinear equations, the population has a simple steady-state solution above threshold (when $n \gg 1$). By setting the time derivative in Eq. (1.1) to zero, one finds $N \cong (K\tau_c)^{-1} = \text{constant}$. That is, the population of the upper laser level is constant above threshold.

Since luminescent intensity depends only on the upper-state population in dielectrics, it follows that spontaneous emission at all wavelengths originating from this excited state should be independent of excitation rate above threshold. Moreover, population clamping above threshold causes amplified emission originating from a common upper state to behave somewhat similarly. In particular, while stimulated emission intensities on competing transitions (with comparable feedback) can sometimes show slow nonlinear increases above threshold, their intensities never decrease with increasing excitation rate as the selected mode grows in standard models.

In light of the universality of population clamping above threshold in laser systems, the quenching of the Nd^{3+}:δ-Al_2O_3 powder laser reported in Ref. 15 is puzzling. These results are reproduced in Fig. 1 to show that the emission intensities on all transitions other than one ($^2F_{5/2}$–$^4F_{9/2}$) quench strongly above a well-defined threshold. That is, their intensities rapidly diminish beyond the point where $^2F_{5/2}$–$^4F_{9/2}$ intensity begins to grow linearly. In the present paper, the origin of this behavior is explained and shown to provide the essential mechanism determining that laser action takes place on the $^2F_{5/2}$–$^4F_{9/2}$ transition. A multilevel extension of the simple laser model above, which includes cascade relaxation among the terminal levels, reveals how long-wavelength stimulated emission processes spoil the inversion on shorter-wavelength transitions from the same

upper level. It predicts strong suppression of gain on shortwave transitions even when the cavity feedback is independent of wavelength. Therefore spectral quenching provides a mechanism determining the output wavelength of random lasers in multilevel systems where multiple inversions and little or no wavelength selectivity exist.

To begin, a simple model is considered in which two transitions compete for gain on coupled stimulated emission transitions in a Λ-type configuration, as shown in Fig. 3(a). Figures 3(a) and 3(b) are models for emission from the $^2F_{5/2}$ level that is populated through electrical excitation in the actual level scheme of Nd^{3+} shown in Fig. 2. Population rate equations are coupled with equations for the photon density at each stimulated emission wavelength, assuming quasi-one-dimensional feedback. A cavity lifetime $\tau_c(\nu) \equiv \gamma_c^{-1}$ is associated with each stimulated transition. This treatment shows that the population inversion ratio on Λ-coupled transitions changes sign as the pumping rate is increased, whereas in V configurations this ratio maintains the same sign. Consequently, only in the Λ system can one induced field grow while another one from the same level eventually quenches. The Λ model can easily be extended to permit a detailed fit of three experimental emission curves on previously assigned transitions from the same upper state $^2F_{5/2}$. In this way, satisfactory agreement is obtained with experimental results, and earlier spectroscopic assignments for the cw Nd^{3+}: δ-Al_2O_3 powder laser are corroborated, lending perspective on additional results in yttria powders and permitting estimation of the average cavity Q and size of these lasers.

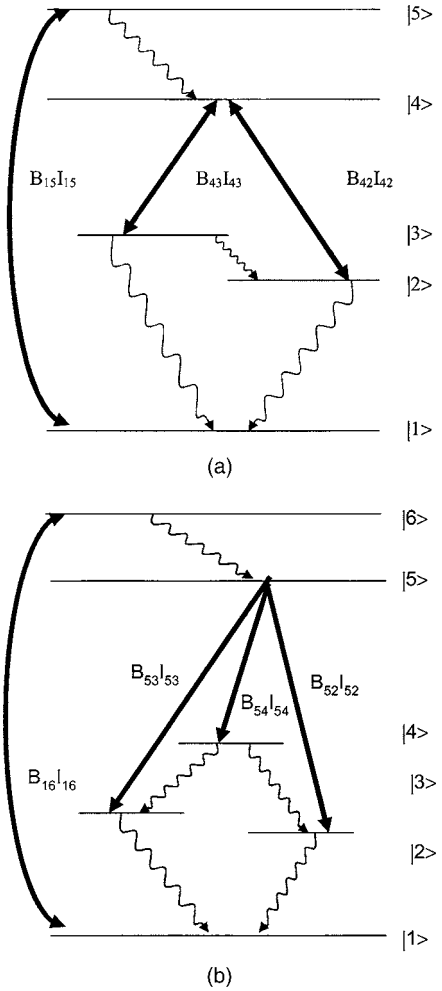

Fig. 3. (a) Simple model for analyzing simultaneous emission on two stimulated transitions in a Λ-type configuration. The pump transition and stimulated emission processes are shown as curved and straight bold arrows, respectively. (b) An extended Λ model with three stimulated emission transitions from the common upper state $^2F_{5/2}$, relevant to observations in Nd^{3+}: δ-Al_2O_3.

Throughout this section, one-dimensional analysis is utilized. As we discuss later, its applicability is determined by the low gain in our experiments. Under active, low-gain conditions, the doubling of coherently backscattered amplitudes is a decisive factor in establishing linear feedback paths for gain-assisted propagation. We believe this accounts for one-dimensional gain-assisted localization rather than diffusive feedback in the experiments reported here.

A. Λ-Type Atom Model

Consider the five-level atom of Fig. 3. Though no population is maintained in the uppermost level (the decay rate constant from level 5 to 4 is taken to be $\gamma_{54}=\infty$), the highest state serves the purpose of pumping the upper states equivalently in a Λ-type model (presented here in detail) or a V-type model (the results for which are merely stated here). Other things being equal, the relative gain on competing stimulated transitions ($4\rightarrow3$ and $4\rightarrow2$) is completely determined by the corresponding inversions $\Delta N_{ij} \equiv N_i - N_j$ between their lower ($i=2,3$) and their upper ($j=4$) levels. In the undepleted pump regime ($N_1 \cong N$), the rate equations are

$$\dot{N}_4 = K_{15} n_{15} N - \gamma_4 N_4 + K_{42} n_{42} \Delta N_{24} + K_{43} n_{43}, \tag{2.1.1}$$

$$\dot{N}_3 = -K_{43} n_{43} \Delta N_{34} + \gamma_{43} N_4 - \gamma_3 N_3, \tag{2.1.2}$$

$$\dot{N}_2 = -K_{42} n_{42} \Delta N_{24} + \gamma_{32} N_3 + \gamma_{42} N_4, \tag{2.1.3}$$

where $N=N_1+N_2+N_3+N_4$.

Corresponding equations for the photon densities are

$$\dot{n}_{43} = -K_{43} \Delta N_{34} n_{43} + K_{43} N_4 - \gamma_{c43} n_{43}, \tag{2.1.4}$$

$$\dot{n}_{42} = -K_{42} \Delta N_{24} n_{43} + K_{42} N_4 - \gamma_{c42} n_{42}. \tag{2.1.5}$$

To identify quenching mechanisms that are not merely the putative result of differences among the rate constants of stimulated transitions but have more universal origins, it is assumed that $K_{43}=K_{42}=K$ and that the feedback mechanism is independent of wavelength ($\gamma_{c43}=\gamma_{c42}\equiv\gamma_c$). Without loss of generality, the model can be further simplified by assuming $\gamma_{42}=\gamma_{41}=\gamma_{31}=0$. Then, by setting the time derivatives on the left-hand side of Eqs. (2.1.1)–(2.1.3) equal to zero, it is straightforward to solve for the ratio of steady-state inversions on the $3\rightarrow4$ and $2\rightarrow4$ transitions:

$$\frac{\Delta N_{34}}{\Delta N_{24}} = \frac{(\gamma_{43} - \gamma_{32})(\gamma_{21} + Kn_{42})}{(\gamma_{32} + Kn_{43})(\gamma_{43} + Kn_{42} + Kn_{43}) - Kn_{43}(\gamma_{43} + Kn_{43}) - (\gamma_{21} + Kn_{42})(\gamma_{32} + Kn_{43})}. \quad (2.1.6)$$

Steady-state solutions for the photon densities are

$$n_{43} = \left(\frac{KN_4}{K\Delta N_{34} + \gamma_c}\right), \quad n_{42} = \left(\frac{KN_4}{K\Delta N_{24} + \gamma_c}\right). \quad (2.1.7)$$

If $\Delta N > 0$, the photon densities are positive. If $\Delta N < 0$, whereupon n_{43} or n_{42} can become arbitrarily large, we see that both inversions clamp at the value $\Delta N = -\gamma_c/K$, ignoring spontaneous emission in Eqs. (2.1.4) and (2.1.5). The photon densities become large but remain positive. To promote lasing in the system, high rates of decay out of the terminal states 2 and 3 ($\gamma_{32}, \gamma_{21} \gg \gamma_{43}$) are desirable. When this is taken into account, the inversion ratio in Eq. (2.1.6) reduces in the weak pump limit to

$$\frac{\Delta N_{34}}{\Delta N_{24}} \cong \frac{-\gamma_{32}\gamma_{21}}{-\gamma_{32}\gamma_{21}} = 1, \quad (2.1.8)$$

while in the strong pump limit, when stimulated emission dominates, we have

$$\frac{\Delta N_{34}}{\Delta N_{24}} = \frac{-\gamma_{32}(\gamma_{21} + Kn_{42})}{-\gamma_{32}(\gamma_{21} + Kn_{42}) + Kn_{43}(Kn_{42} - \gamma_{21})}. \quad (2.1.9)$$

In Eq. (2.1.9) the inversion on the short-wavelength transition (ΔN_{24}) changes sign with increasing excitation rate, becoming absorptive, when the denominator is positive (i.e., when $K^2 n_{43} n_{42} > \gamma_{32}\gamma_{21} + \gamma_{32}Kn_{42} + \gamma_{21}Kn_{43}$). Consequently, gain is eventually quenched on the short-wavelength transition in the Λ configuration, despite the assumed equality of Einstein A and B coefficients on the emissive transitions [$4 \rightarrow 3$ and $4 \rightarrow 2$ in Fig. 3(a)]. A straightforward adaptation of this analysis to V-type configurations shows that with a common terminal level, instead of a common initial level, quenching does not take place. Similarly, in systems where there are no common levels at all, there are no coupling (quenching) effects.

B. Λ Configuration—Three Stimulated Transitions

To permit a detailed comparison between theoretical and experimental emission intensities on the three observed $^2F_{5/2}$ transitions in Nd^{3+}:δ-Al_2O_3 nanopowder samples, the basic Λ model of Subsection 2.A must include three stimulated emission transitions with feedback [Fig. 3(b)] as follows:

$$N_1 + N_2 + N_3 + N_4 + N_5 + N_6 = N, \quad (2.2.1)$$

$$\dot{N}_6 = R_p(N_1 - N_6) - \gamma_{65}N_6, \quad (2.2.2)$$

$$\dot{N}_5 = -(\gamma_{54} + \gamma_{53} + \gamma_{52})N_5 + \gamma_{65}N_6 + K_{53}(N_4 - N_5)n_{54} + K_{53}(N_3 - N_5)n_{53} + K_{52}(N_2 - N_5)n_{52}, \quad (2.2.3)$$

$$\dot{N}_4 = \gamma_{54}N_5 - \gamma_{41}N_4 - \gamma_{42}N_4 - \gamma_{43}N_4 - K_{54}(N_4 - N_5)n_{54}, \quad (2.2.4)$$

$$\dot{N}_3 = \gamma_{53}N_5 - \gamma_{31}N_3 - \gamma_{32}N_3 + \gamma_{43}N_4 - K_{53}(N_3 - N_5)n_{53}, \quad (2.2.5)$$

$$\dot{N}_2 = \gamma_{52}N_5 - \gamma_{21}N_2 + \gamma_{42}N_4 + \gamma_{32}N_3 - K_{52}(N_2 - N_5)n_{52}, \quad (2.2.6)$$

$$\dot{N}_1 = -R_p(N_1 - N_6) + \gamma_{41}N_4 + \gamma_{31}N_3 + \gamma_{21}N_2, \quad (2.2.7)$$

$$\dot{n}_{54} = -K_{54}n_{54}(N_4 - N_5) + K_{54}N_5 - \gamma_{c54}n_{54}, \quad (2.2.8)$$

$$\dot{n}_{53} = -K_{53}n_{53}(N_3 - N_5) + K_{53}N_5 - \gamma_{c53}n_{53}, \quad (2.2.9)$$

$$\dot{n}_{52} = -K_{52}n_{52}(N_2 - N_5) + K_{52}N_5 - \gamma_{c52}n_{52}. \quad (2.2.10)$$

Steady-state emission intensities were calculated using Eqs. (2.2.1)–(2.2.10) versus excitation rate on transitions from initial state $^2F_{5/2}$ to terminal states $^4F_{9/2}$, $^4F_{3/2}$, and $^4I_{15/2}$ for comparison with the data of Fig. 1. The decay rate constants for weak processes were set to zero ($\gamma_{31} = \gamma_{41} = 0$), and cavity feedback was assumed to be the same ($\gamma_{c54} = \gamma_{c53} = \gamma_{c52} \equiv \gamma_c$) for all wavelengths. The decay constants on the coupled transitions were determined from the initial slopes in Fig. 1 to be in the ratio of $\gamma_{53}/\gamma_{52} = 2.1/4.3$ for $^2F_{5/2} \rightarrow {}^4F_{3/2}$ and $^4I_{15/2}$, respectively. Since saturation effects are evident in the $^2F_{5/2} - {}^4F_{9/2}$ transition data (Fig. 1), the calculations included ground-state depletion. Five parameters were adjusted to fit the data for all three curves simultaneously, namely, the radiative decay rate γ_{54} from the $^2F_{5/2}$ state, the decay rates between terminal levels of the coupled states ($\gamma_{43} = \gamma_{42}$), the rate of decay from the terminal level to ground ($\gamma_{31} = \gamma_{21}$), the cavity decay rate γ_c, and the cavity size l_c.

C. Theoretical Nature of the Effective Cavities

Prior calculations of propagation in porous alumina powders[16] showed that large electric field enhancements are possible inside random one-dimensional dielectrics when a plane wave is incident on the sample, from the outside. As shown in Fig. 4, similar results are obtained when the field is a dipole source located within the sample, corresponding closely with the situation in our electron-beam experiments.

In one dimension, correlated scattering can create regions where the field emitted by a dipole is enhanced by factors up to 100 under the same conditions of average particle spacing and refractive index as in our experiments. Figure 4(a) presents a field map for light of wavelength $\lambda = 400$ nm, based on one configuration of dielectric layers and spaces that achieves a field enhancement of this magnitude. Different sample configurations were determined randomly as described in Ref. 16 with mean center-to-center particle spacing of 80 nm, average diameter $\phi = 40$ nm, $n = 1.78$, and square distributions of particle size and spacing having FWHM values of 10 and

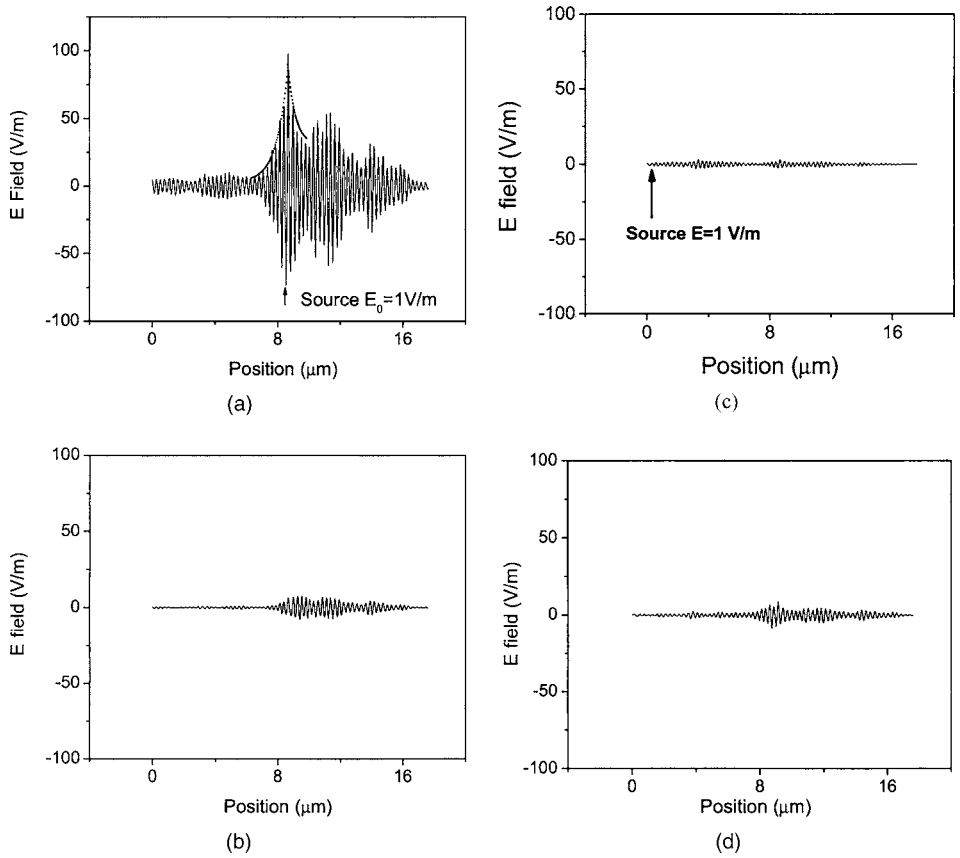

Fig. 4. Exact calculation of the electric field inside a random one-dimensional medium with the average properties in the experiment (see text) for (a) a random particle configuration that achieves an enhancement $|E(z)/E(0)|$ of 100 relative to a 400 nm dipole source located at the arrow, (b) with the wavelength changed to 402 nm, (c) the same configuration with the dipole repositioned, and (d) after removal of a 0.48 μm thickness from the left side of the sample ($\lambda = 400$ nm). The dashed curve in (a) outlines exponential decay of the field envelope in one location, showing energy localization on a length scale close to the wavelength.

20 nm, respectively. Configurations were tested individually for enhancement. The trace in Fig. 4(b) confirms that the source of cavity effects is interference, since the field enhancement drops dramatically when the wavelength is altered by only 0.5%. Also, for the same configuration as in Fig. 4(a), enhancement is greatly reduced when the source dipole position is altered by $\sim 20\lambda$ [Fig. 4(c)], suggesting that the enhancement effect is not associated with any regular structure at a specific location within the medium. This conclusion is confirmed by the trace of Fig. 4(d) where a thin multilayer (0.48 μm thick) is removed from the left surface of the medium and the enhancement of the centered dipole is then recalculated. Despite the remoteness of the structural change from both the source and the enhancement region shown in Fig. 4(a), the field enhancement is lost, showing that it is a global property of the sample.

Figure 5(a) shows that the bandwidth of the energy density enhancement $|E(z)/E_0|^2_{\max}$ is $\Delta\lambda = 0.68$ nm (FWHM), corresponding to a passive cavity quality factor of $Q = 2\pi\lambda/\Delta\lambda = 3694$. A second theoretical estimate of Q for the same configuration was obtained by solving finite-difference time-domain (FDTD) Maxwell equations together with the polarization equation (see Ref. 9). First, when gain was included, the one-dimensional FDTD code predicted the observed laser threshold within a factor of 3.[20] Then when gain was omitted, the electric field evolution initiated by a short pulse ($\tau_p < 200$ fs) from the internal dipole yielded the field decay curve in Fig. 5(b), from which a $1/e$ energy decay time of $\tau_{\mathrm{FDTD}} = 0.80$ ps and $Q_{\mathrm{FDTD}} = \omega\tau_{\mathrm{FDTD}} = 4039$ were deduced. Thus good agreement with the Q value based on bandwidth was obtained. The importance of global interference in establishing this high Q is reinforced in Fig. 6, where calculations of density–density correlations for three different interface configurations (with the same particle spacing of 80 nm) are shown. The first peak in each trace of Fig. 6 merely gives the average particle spacing, as we confirmed with other calculations at different densities. No other reproducible density correlations versus distance (identifiable structures) are apparent, whether a large enhancement is present or not. We conclude that large field enhancements result from long-range, collective (multiple-scattering) interference effects.

3. EXPERIMENTS

Spectral quenching and laser action were observed in Nd^{3+}:δ-Al_2O_3 nanopowder samples using electron-beam irradiation in ultrahigh vacuum. Experimental details have been described previously.[15] After dispersion by a grating spectrometer, optical emission intensities were recorded versus beam current using photon counting. As shown in Fig. 1, one spectral line was found to have a dis-

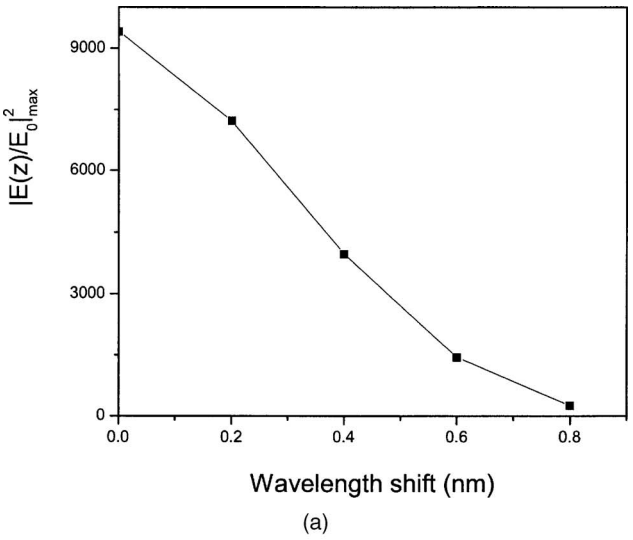

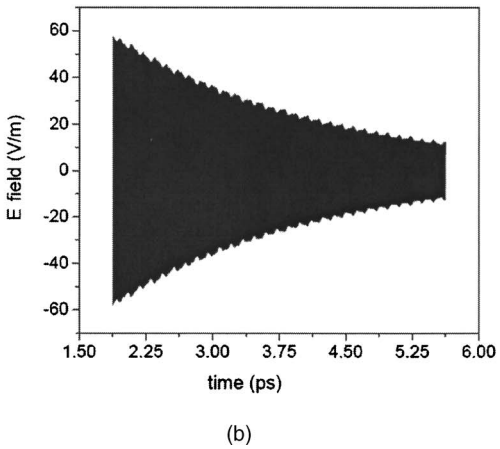

Fig. 5. (a) Exact computation of $|E(z)/E(0)|^2_{max}$ versus wavelength (λ_0=400 nm) for the particle configuration of Fig. 4(a). (b) Temporal decay of the electric field of a pulsed dipole source in the enhancement zone of Fig. 4(a), calculated by the FDTD in response to a square pulse of duration τ=200 fs (with zero gain).

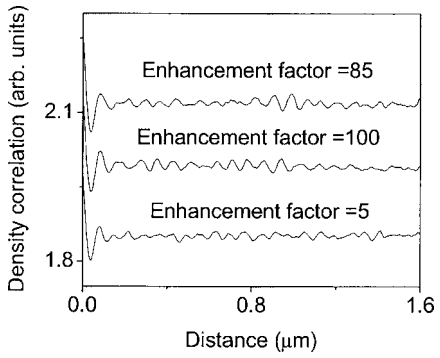

Fig. 6. Density–density correlations for three different particle configurations that achieve field enhancements of 85, 100, and 5 for the upper, middle, and lower curves, respectively. Average interparticle spacing was 80 nm. The (unnormalized) density correlation was 2.1 at the origin in all cases; the curves have been shifted vertically for presentation.

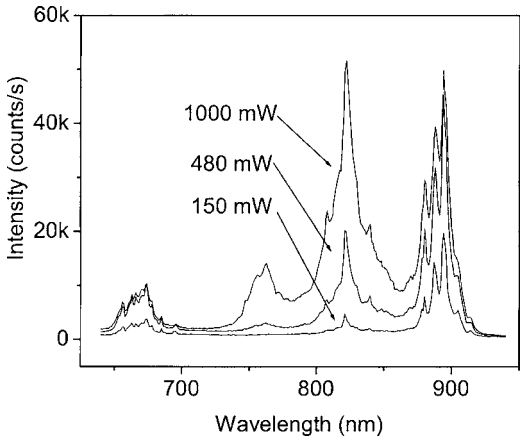

Fig. 7. Emission spectra from optically excited Nd^{3+}:Y_2O_3 nanopowder, irradiated with Ar laser powers of 150, 480, and 1000 mW at a wavelength of λ_{ex}=514.5 nm.

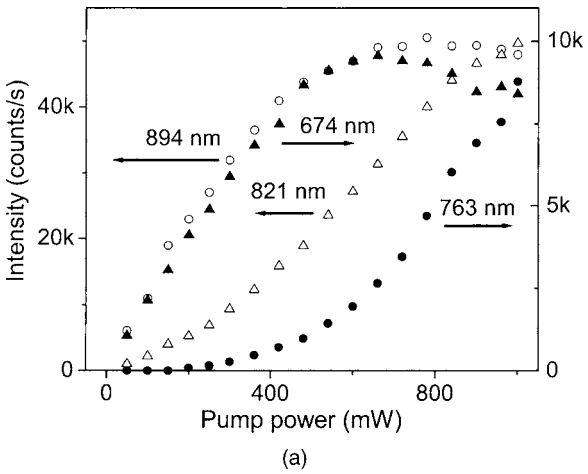

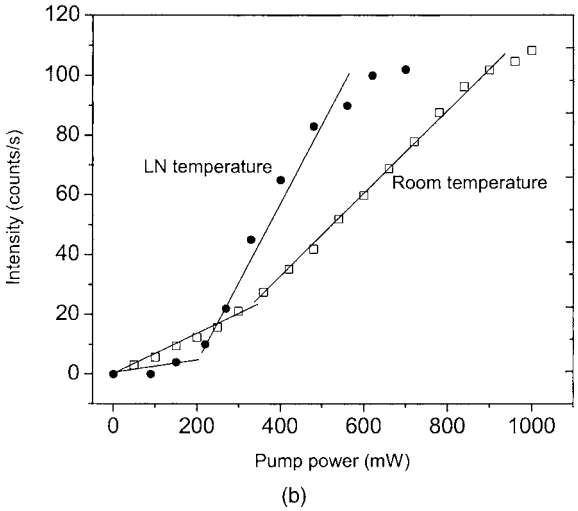

Fig. 8. (a) Peak emission intensity from optically excited Nd^{3+}:Y_2O_3 nanopowder at four wavelengths versus incident laser power (λ_{ex}=514.5 nm, spot diameter of ϕ=0.1 mm) at room temperature, and (b) a comparison of output curves at low (T=77 K) and high (T=295 K) temperatures on the 821 nm transition, showing the change in threshold and slope. Solid curves are guides to the eye. LN, liquid nitrogen.

tinct threshold, whereas all other lines from the same upper state intensified from the beginning, passed through a peak near threshold, and then decreased in intensity. No spectral line narrowing was observed, consistent with expectations for a low-gain laser having an effective cavity size of the order of the wavelength.

We also achieved cw laser action in $Nd^{3+}:Y_2O_3$ samples by using optical excitation with the 514.5 nm line of the Ar^+ laser, as shown by the sudden appearance of new spectral features at high excitation rates (Fig. 7). In these experiments, sample luminescence caused by a normally incident beam was collected from flat nanopowder surfaces at room temperature and analyzed using a 0.25 m/*f*3.7 grating spectrometer at several incident powers. The Nd^{3+} transitions whose peak intensities are plotted in Fig. 8(a) are different from those in Fig. 1. The photon energy at 514 nm is not adequate to populate the high-lying ^2F states responsible for the cathodoluminescence of Fig. 1. Excitation instead takes place via the resonant ground-state optical absorption $^4I_{15/2}-{}^4G_{9/2}$ of Nd^{3+} (see Fig. 2). Figure 8(b) shows low-temperature (T = 77 K) data on the best isolated transition at 821 nm.

Previous spectroscopy[21–26] of single-crystal $Nd^{3+}:Y_2O_3$ permitted assignment of the 763 and 821 nm emissions despite the presence of overlapping lines and large inhomogeneous broadening. As discussed in more detail in Appendix A, these lines are ascribed to the $(^4G_{7/2}+{}^2K_{13/2}) \rightarrow {}^4I_{15/2}$ and $(^4F_{5/2}+{}^2H_{9/2}) \rightarrow {}^4I_{9/2}$ transitions. (Transitions in $Nd^{3+}:Al_2O_3$ were assigned in Ref. 15.) The spectroscopic assignments of the 763 and 821 nm transitions in $Nd^{3+}:Y_2O_3$ indicate that these emission features do not share a common initial or final state.

4. DISCUSSION AND CONCLUSIONS

In Fig. 9 the emission intensities on transitions originating from the $^2F_{5/2}$ state in $Nd^{3+}:\delta\text{-}Al_2O_3$ are compared with theoretical fits based on the results of Subsection 2.C. The Λ model closely reproduces the dramatic quenching on two transitions and the onset of lasing observed on the third transition in $Nd^{3+}:\delta\text{-}Al_2O_3$, with essentially one free parameter per curve. Hence the results are in excellent accord with the quenching of short-wavelength-induced transitions by longer-wavelength transitions from the common upper state, resulting in oscillation at the longest wavelength of the Λ system. The parameter values that yielded the best agreement in the experimental fit of Fig. 9 were $\gamma_{54}=(0.8\pm0.1)\times10^5\ s^{-1}$, $\gamma_{43}=\gamma_{42}=(9\pm1)\times10^7\ s^{-1}$, $\gamma_{21}=\gamma_{31}=(1.8\pm0.2)\times10^6\ s^{-1}$, $\gamma_c=(30\pm10\ ps)^{-1}$ for the cavity decay rate, and $l_c=(1.6\pm0.6)\lambda$ for the effective cavity length at 405 nm. Rate parameters that were fixed in proportion to γ_{54} through observed ratios of luminescence slopes (Fig. 1) together with a previous experimental value[16] for the total $^2F_{5/2}$ decay time ($\gamma_5=4.8\times10^5\ s^{-1}$) were $\gamma_{52}=(3.0\pm0.5)\times10^5\ s^{-1}$ and $\gamma_{53}=(1.0\pm0.3)\times10^5\ s^{-1}$.

Since precise spectroscopic data were unavailable for single-crystal $Nd^{3+}:Al_2O_3$ and there was experimental overlap between $^2F_{5/2}$ and $^2F_{7/2}$ emissions around 400 nm, it is significant that agreement between theory and experiment is achieved only with the Λ coupling specified by earlier upper-state assignments.[15] The apparent success

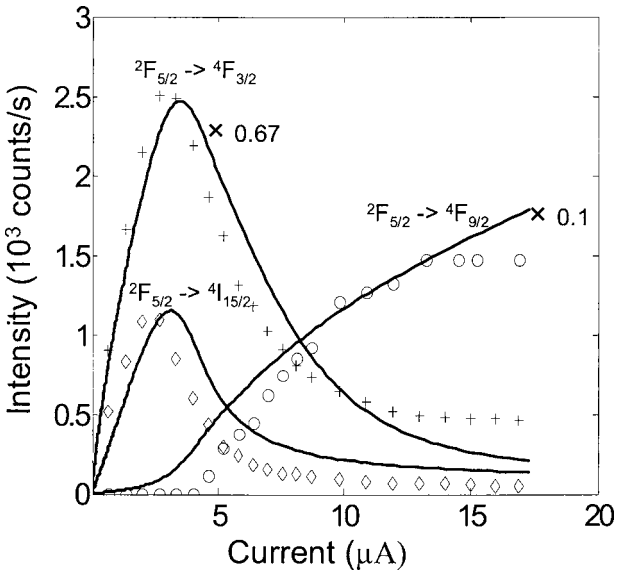

Fig. 9. Observed emission intensity (points) and theoretical predictions (solid curves) for stimulated emission on three coupled transitions in $Nd^{3+}:\delta\text{-}Al_2O_3$. The storage time determined by the fit is $\tau_c=30$ ps, and average cavity size is $l_c=(1.6\pm0.6)\lambda$ at $\lambda=405$ nm. Other fit parameters are given in the text.

of the one-dimensional model is also significant, since the medium is three dimensional. In FDTD simulations, when the dimensionality is increased from one to two dimensions, attainable cavity Q values drop by more than a factor of 20 (Ref. 27). The implication of this trend is that continuous energy storage cannot take place in passive three-dimensional media or media where the gain–length product is much less than 1—like the nanopowders studied in this research—unless the dimensionality is actively restricted to one dimension.

This, in turn, suggests there is a mechanism that reduces the dimensionality of electromagnetic propagation in low-gain random media. We propose that this mechanism is the doubling of the stimulated emission rate and phase retrieval of reflected wave amplitudes that propagate in the exact opposite direction of amplified forward waves in low-gain random media, owing to the phenomenon of coherent backscattering. In the absence of such a mechanism to render the gain extraction path one dimensional, existing theories of localization cannot in fact account for the quality factor $Q>1000$ needed to overcome the deficiency in the stimulated emission cross section σ_{SE} of Nd in our experiments. Over distances of $l=l_c=\lambda$, as determined independently by electron penetration in Ref. 16, the gain–length product must meet the condition $N\sigma_{eff}l_c>1$ for lasing to occur. This requires $Q>1000$, which cannot be accounted for in two or three dimensions. We note, however, that such a mechanism for the reduction of effective dimensionality would not be operative in high-gain random laser media where doubling of the gain for backscattered light would have a negligible effect.

Rate equation analysis of uncoupled transitions (Subsection 2.B) was also in accord with experimental findings in $Nd^{3+}:Y_2O_3$ nanopowder. Using optical pumping, two sets of laser transitions in this host oscillated simultaneously, namely, $(^4G_{7/2}+{}^2K_{13/2}) \rightarrow {}^4I_{15/2}(1)$ and $(^4F_{5/2}+{}^2H_{9/2}) \rightarrow {}^4I_{9/2}(3)$, with experimental thresholds of 200

and 500 mW at room temperature, respectively [see Fig. 8(a)]. The difference in these two threshold values confirms that the nonlinear emissions are neither coupled nor thermal in origin. With an upper-level separation on the 763 and 821 nm transitions[21] of 6159 cm^{-1}, both lines ought to show intensity changes with respect to other lines only if the sample temperature were to rise suddenly above ~8800 K, and such changes should occur simultaneously. Yet the output curves at 763 and 821 nm have different thresholds, and no melting of the samples took place, indicating that temperatures were certainly always less than the melting temperature 2410°C. By calculating the maximum temperature rise possible at the sample surface with the thermal diffusion equation, taking surface albedo, beam size, sample holder geometry, and conductivity into account as in Ref. 28, one finds $\Delta T < 20°C$. This eliminated the possibility that thermal changes in nonradiative relaxation rates played any role in the dynamics reported here.

In agreement with the spectroscopic assignments of Appendix A, there was no evidence that the transitions at 763 and 821 nm in $Nd^{3+}:Y_2O_3$ had common upper or lower states. Consequently, these transitions should be independent, capable of simultaneous laser action, and free of coupling effects. Indeed, no quenching was observed. These results therefore complement those in $Nd^{3+}:Al_2O_3$ by demonstrating that cw random laser action may be achieved by electrical or optical means, that feedback from multiple scattering is effective over a wide range of wavelengths, and that quenching can arise in the presence of coupled dynamics on multiple inverted transitions. The present results in $Nd^{3+}:Y_2O_3$ and earlier measurements[29] of transport lengths in Al_2O_3 show little wavelength dependence in the scattering feedback. Hence the analysis of spectral quenching in $Nd^{3+}:Al_2O_3$ identifies a mechanism that favors long-wavelength laser transitions whenever there is gain competition with Λ coupling.

In summary, nonlinear rate equation and FDTD analysis can account quantitatively for experimental spectral quenching, threshold behavior, output power, and saturation of electrically pumped cw ultraviolet laser action in $Nd^{3+}:\delta$-Al_2O_3 nanopowder. We conclude that the spectral quenching phenomenon results from upper-state coupling of induced emissive transitions in the presence of strong scattering. From the highly constrained fit to multiple $^2F_{5/2}$ output curves, an energy storage time of $\tau_c = (30 \pm 10)$ ps is deduced, together with an average (cubic) cavity length of $l_c = (1.6 \pm 1.0)\lambda$ that shows light is confined to roughly a single spatial period. The time reported above for bright storage of stationary light is 22 000 times longer than the period of time 405 nm light would normally spend in a wavelength-sized region in free space. Results presented here for $Nd^{3+}:Y_2O_3$ nanopowder also demonstrate that optical pumping can be used to achieve cw random laser action on two transitions simultaneously, again in agreement with semiclassical laser theory.

APPENDIX A

Transition assignments for photoluminescence spectra of $Nd:Y_2O_3$ nanopowders excited at $\lambda_{ex} = 514.5$ nm (19,436 cm^{-1}) were based on prior spectroscopy.[25,26] By consideration of all energetically allowed candidates for the upper level, possible assignments for transitions yielding wavelengths of observed peaks near 821 and 763 nm (to within 50 cm^{-1}) were compiled and compared with experiment in Tables 1 and 2. All four peaks near 821 nm are accounted for as $(^4F_{5/2} + {}^2H_{9/2}) \rightarrow {}^4I_{9/2}$ within ±2 nm. For 763 nm emission, two assignments can account, in principle, for the observed lines within ±2 nm, namely, $(^4G_{7/2} + {}^2K_{13/2}) \rightarrow {}^4I_{15/2}$ or $(^2G_{7/2} + {}^4G_{5/2}) \rightarrow {}^4I_{13/2}$. Neither of these latter two transitions shares a common level with the 821 nm assignment. On the basis of the energy-gap law, the first of these is the more radiative. Hence the final assignment of the 763 nm line is $(^4G_{7/2} + {}^2K_{13/2}) \rightarrow {}^4I_{15/2}$.

ACKNOWLEDGMENTS

Support for this research was provided by the Air Force Office of Scientific Research (F49620-03-1-0389) and the

Table 1. Calculated and Observed Luminescent Peak Positions near 821 nm in $Nd:Y_2O_3$

Initial State	Energy (cm^{-1})	Final State	Energy (cm^{-1})	Calculated λ_T (nm)	Experimental λ_E (nm)	Difference $\Delta = \lambda_T - \lambda_E$
$^4F_{5/2} + {}^2H_{9/2}(7)$	12,642	$^4I_{9/2}(4)$	447	820	821	−1
$^4F_{5/2} + {}^2H_{9/2}(7)$	12,642	$^4I_{9/2}(3)$	269	808	808	0
$^4F_{5/2} + {}^2H_{9/2}(3)$	12,395	$^4I_{9/2}(3)$	447	836	839	−3
$^4F_{5/2} + {}^2H_{9/2}(6)$	12,533	$^4I_{9/2}(3)$	269	815	817	−2

Table 2. Calculated and Observed Luminescent Peak Positions near 763 nm in $Nd:Y_2O_3$

Initial State	Energy (cm^{-1})	Final State	Energy (cm^{-1})	Calculated λ_T (nm)	Experimental λ_E (nm)	Difference $\Delta = \lambda_T - \lambda_E$
$^2G_{7/2} + {}^4G_{5/2}(3)$	16,902	$^4I_{13/2}(1)$	3814	764	763	1
$^2G_{7/2} + {}^4G_{5/2}(2)$	16,767	$^4I_{13/2}(1)$	3840	773	775	−2
$^2G_{7/2} + {}^2K_{13/2}(5)$	18,793	$^4I_{15/2}(1)$	5709	764	763	1
$^2G_{7/2} + {}^2K_{13/2}(2)$	18,592	$^4I_{15/2}(1)$	5709	776	775	1

National Science Foundation (DMR-0502715, CISE 0531086). Any opinions, findings, and conclusions are those of the authors and do not necessarily reflect the views of the National Science Foundation.

S. C. Rand, the corresponding author, can be reached by e-mail at scr@umich.edu.

REFERENCES

1. V. M. Markushev, V. F. Zolin, and C. M. Briskina, "Luminescence and stimulated emission of neodymium in sodium lanthanum molybdate powders," Sov. J. Quantum Electron. **16**, 281–283 (1986).
2. C. Gouedard, D. Husson, C. Sauteret, F. Auzel, and A. Migus, "Generation of spatially incoherent short pulses in laser-pumped neodymium stoichiometric crystals and powders," J. Opt. Soc. Am. B **10**, 2358–2363 (1993).
3. M. A. Noginov, N. E. Noginova, H. J. Caulfield, P. Vankateswarlu, T. Thompson, M. Mahdi, and V. Ostroumov, "Short-pulsed stimulated emission in the powders of $NdAl_3(BO_3)_4$, $NdSc_3(BO_3)_4$, and $Nd:Sr_5(PO_4)_3F$ laser crystals," J. Opt. Soc. Am. B **13**, 2024–2033 (1996).
4. N. M. Lawandy, R. M. Balachandran, A. S. L. Gomes, and E. Sauvain, "Laser action in strongly scattering media," Nature **368**, 436–438 (1994).
5. S. V. Frolov, Z. V. Vardeny, K. Yoshino, A. Zhakidov, and R. H. Baughman, "Stimulated emission in high-gain organic media," Phys. Rev. B **59**, R5284–R5287 (1999).
6. H. Cao, Y. G. Zhao, S. T. Ho, E. W. Seelig, Q. H. Wang, and R. P. H. Chang, "Random laser action in semiconductor powder," Phys. Rev. Lett. **82**, 2278–2281 (1999).
7. R. K. Thareja and A. Mitra, "Random laser action in ZnO," Appl. Phys. B **71**, 181–184 (2000).
8. C. Vanneste and P. Sebbah, "Selective excitation of localized modes in active random media," Phys. Rev. Lett. **87**, 183903 (2001).
9. X. Jiang and C. Soukoulis, "Transmission and reflection studies of periodic and random systems with gain," Phys. Rev. B **59**, 6159–6166 (1999).
10. R. C. Polson, A. Chipouline, and Z. V. Vardeny, "Random lasing in π-conjugated films and infiltrated opals," Adv. Mater. (Weinheim, Ger.) **13**, 760–764 (2001).
11. M. A. Noginov, S. U. Egarievwe, N. Noginova, H. J. Caulfield, and J. C. Wang, "Interferometric studies of coherence in a powder laser," Opt. Mater. **12**, 127–134 (1999).
12. H. Cao, Y. Ling, J. Y. Xu, C. Q. Cao, and P. Kumar, "Photon statistics of random lasers with resonant feedback," Phys. Rev. Lett. **86**, 4524–4527 (2001).
13. R. M. Laine, T. Hinklin, G. Williams, and S. C. Rand, "Low-cost nanopowders for phosphor and laser applications by flame spray pyrolysis," Mater. Sci. Forum **344–346**, 500–510 (2000).
14. G. R. Williams, B. Bayram, S. C. Rand, T. Hinklin, and R. M. Laine, "Laser action in strongly scattering rare-earth-metal-doped dielectric nanophosphors," Phys. Rev. A **65**, 013807 (2001).
15. B. Li, G. R. Williams, S. C. Rand, T. Hinklin, and R. M. Laine, "Continuous-wave ultraviolet laser action in strongly scattering Nd-doped alumina," Opt. Lett. **27**, 394–396 (2002).
16. S. M. Redmond, G. L. Armstrong, H.-Y. Chan, E. Mattson, A. Mock, B. Li, J. R. Potts, M. Cui, S. C. Rand, S. L. Oliveira, J. Marchal, T. Hinklin, and R. M. Laine, "Electrical generation of stationary light in random scattering media," J. Opt. Soc. Am. B **21**, 214–222 (2004).
17. S. John and R. Rangarajan, "Optimal structures for classical wave localization: an alternative to the Ioffe–Regel criterion," Phys. Rev. B **38**, 10101–10104 (1988).
18. J. Bertolotti, S. Gottardo, D. S. Wiersma, M. Ghulinyan, and L. Pavesi, "Optical necklace states in Anderson localized 1D systems," Phys. Rev. Lett. **94**, 113903 (2005).
19. See, for example, A. E. Siegman, *Lasers* (University Science, 1986), p. 515.
20. B. Li, "Continuous-wave laser action in random scattering media," Ph.D. dissertation (University of Michigan, 2006).
21. N. C. Chang, "Energy level and crystal field splittings of Nd^{3+} in yttrium oxide," J. Chem. Phys. **44**, 4044–4050 (1966).
22. W. F. Krupke, "Optical absorption and fluorescence intensities in several rare-earth-doped Y_2O_3 and LaF_3 single crystals," Phys. Rev. **145**, 325–337 (1966).
23. G. M. Zverev, G. Ya. Kolodnyi, and A. I. Smirnov, "Optical spectra of Nd^{3+} in single crystals of scandium and yttrium oxides," Opt. Spectrosc. **23**, 325–327 (1967).
24. M. J. Weber, "Radiative and multiphonon relaxation of rare-earth ions in Y_2O_3," Phys. Rev. **171**, 283–291 (1968).
25. B. M. Walsh, J. M. McMahon, W. C. Edwards, N. P. Barnes, R. W. Equall, and R. L. Hutcheson, "Spectroscopic characterization of $Nd:Y_2O_3$: application toward a differential absorption lidar system for remote sensing of ozone," J. Opt. Soc. Am. B **19**, 2893–2903 (2002).
26. J. Stone and C. A. Burrus, "$Nd:Y_2O_3$ single-crystal fiber laser: room-temperature cw operation at 1.07- and 1.35-μm wavelength," J. Appl. Phys. **49**, 2281–2287 (1978).
27. X. Ruan and M. Kaviany, "Photon localization and electromagnetic field enhancement in laser-irradiated, random porous media," Microscale Thermophys. Eng. **9**, 63–84 (2005).
28. S. Redmond, S. C. Rand, X. L. Ruan, and M. Kaviany, "Multiple scattering and nonlinear thermal emission of Yb^{3+},$Er^{3+}:Y_2O_3$ nanopowders," J. Appl. Phys. **95**, 4069–4077 (2004).
29. S. C. Rand, "Strong localization of light and photonic atoms," Can. J. Phys. **78**, 625–637 (2000).